Submesoscale air-sea interactions as revealed by SWOT

M. Kaouah[1,2], G. Lapeyre[1], L. Renault[2], X. Perrot[1] and C. Dablemont[3]

[1]LMD-IPSL, ENS, Université PSL, Sorbonne Université, CNRS, Paris, France
[2]Université de Toulouse, LEGOS (CNES/CNRS/IRD/UPS), Toulouse, France
[3]Institut des Sciences Moléculaires d'Orsay (ISMO), CNRS, Université Paris-Saclay, France

Key Points:

- We assess the capability of the satellite SWOT to measure air-sea interactions from space
- We document a case in the Gulf Stream region during which different ocean and atmosphere satellite products were available
- Sea surface temperature anomalies affect surface winds at scales of a few kilometers

Corresponding author: Guillaume Lapeyre, `guillaume.lapeyre@sorbonne-universite.fr`

Abstract

At midlatitudes, air-sea interactions have been documented in numerical models, in situ campaigns and satellite observations down to the ocean mesoscales. However little is known about scales of a few kilometers (the submesoscales). The new satellite mission SWOT provides a global coverage of these scales by measuring sea surface height. In addition, it provides surface wind speeds at the same resolution. Here, we take profit of this new dataset to examine a particular situation in the Gulf Stream area when scatterometer winds, SST and Chlorophyll at kilometer scales were available. A good correspondence between winds from SWOT and scatterometers is found at the mesoscales. More importantly, we show that SWOT detects submesoscale features of 10 km scales, correlated with SST anomalies and Chlorophyll. We conclude that SWOT will be a tremendous instrument for air-sea interactions studies through its surface wind measurements.

Plain Language Summary

The Surface Water and Ocean Topography (SWOT) mission has been designed to monitor the global ocean at fine scales (i.e. down to a few kilometers) through the measure of sea surface height (from which ocean currents can be computed). However, SWOT's capability is not limited to this, since it also provides other important climate variables, such as surface winds. This suggests the possibility to better understand the relation between the ocean and the atmosphere at fine scales. In the Gulf Stream region, using SWOT's dataset as well as other satellite products, we show that there is a high correlation between sea surface temperature and winds, with weaker winds above cold oceanic fine scales. Such a result agrees with theoretical mechanisms about the effect of the ocean on the atmosphere on scales of hundreds of kilometers. We then conclude that SWOT is a powerful tool to document air-sea interactions at kilometer scales from space.

1 Introduction

Oceanic submesoscale currents (corresponding to scales O(10)km) have received considerable attention in the last two decades for their non-negligible role in the climate system (see reviews by Klein & Lapeyre, 2009; McWilliams, 2016; Taylor & Thompson, 2023, among others). In particular, they significantly influence vertical and horizontal fluxes of heat and biogeochemical materials (Su et al., 2018; Lévy et al., 2018) and also modulate the oceanic forward and inverse energy cascades (Klein et al., 2008; Capet et al., 2008). However, the interactions of submesoscale flows with the atmosphere remain poorly understood, likely due to technical limitations such as model and satellite resolution, as well as the challenges of capturing these features with ship-based campaigns. Nevertheless, growing evidence in the recent literature underscores their importance in modulating the atmospheric variability. For example, Song et al. (2022) used in-situ data in the Western Pacific and showed variations of latent heat flux anomalies of O(10) W m^{-2} over a submesoscale fronts of O(5) km. Shao et al. (2019) made similar observations using in situ data in the Gulf of Mexico. In addition, this latter study documented variations in wind speed of 1 m s^{-1} for a 1.5 °C variation in sea surface temperature (SST) over 6 km. Using numerical models resolving submesoscales, Strobach et al. (2022) and Wenegrat and Arthur (2018) showed that the Marine Atmospheric Boundary Layer (MABL) actually responds at the same scale as oceanic features. As shown by Vivant et al. (2025), the response is not limited to the MABL but extends to the whole troposphere as moist convection was found to be triggered above submesoscale fronts over the passage of mid-latitude storms. Other numerical studies by Bai et al. (2023), Conejero et al. (2024), and Renault et al. (2024) revealed the effect of submesoscale ocean currents on the wind and surface heat fluxes.

Satellite observations of such submesoscales dynamics are until now very limited and remain a challenge (Klein et al., 2019). Using high-resolution (100 m) thermal sensors, Gaube et al. (2019) were able to identify a submesoscale feature with a 13° C gradient over just 15 km, along with a 2 m/s wind anomaly associated with it. But this study was limited as only data close to the coast of the North-West Atlantic were available. The Surface Water and Ocean Topography (SWOT) mission launched in December 2022 (Morrow et al., 2019; Fu et al., 2024) now provides two-dimensional maps of sea surface height (SSH) and ocean surface roughness with a spatial resolution of 2 km. First studies have shown that the SWOT mission will help in better characterizing the submesoscale currents (Zhang et al., 2024). Here, our primary goal is to highlight the potential of SWOT in documenting air-sea interactions at fine scales through its associated surface wind product. In combination with traditional satellite datasets, such as SST and chlorophyll concentrations, which have similar spatial resolution, we present evidence of the signature of SST anomalies on the surface wind at submesoscales for a particular situation in the Gulf Stream region.

2 Data

We focus our study on a particular atmospheric situation during the 1-day repeat period of the SWOT mission, which occurred between March 29 and July 11, 2023. On May 12, the SWOT satellite passed over the Gulf Stream region near 36°N, 74°W (see Fig. 1a and e for the studied region and for the swath covered by SWOT), corresponding to pass 9, cycle 519. We use the L2 product (PGC0, as of 01/10/2024), which provides 10-m equivalent neutral wind (ENW) speed relative to the surface current with a resolution of 2 km (Stiles et al., 2024). Note that wind directions cannot be retrieved as the measurements are acquired from a single azimuth.

This dataset is compared with scatterometer measurements from the MetOp-B ASCAT-L2-Coastal products (Verhoef et al., 2012) which also provide 10 m ENW relative to the surface current, but with a nominal spatial resolution of 12.5 km, allowing to capture the oceanic mesoscales. Only a few snapshots were available in the time range ±12h from the SWOT measurements, one at 15:17 UTC on May 12 and one at 2:35 UTC on May 13.

In addition, we use the 10 m winds of the (HRES) ECMWF forecast model (cycle 47r3), which has a spatial resolution of about 9 km at mid-latitudes. It is coupled to ocean model NEMO (version 3.4), which is run at a resolution of 1/4° (about 28 km at mid-latitudes) and initialized with daily SST analyses from OSTIA (re-gridded at 1/4°). Hence the ocean model is only mesoscale eddy-permitting, and therefore does not fully resolve the full spectrum of oceanic mesoscales (and obviously not the submesoscales). We thus expect air-sea interactions not to be completely resolved at mesoscales by the coupled model. Note that the effect of surface currents on the atmosphere (e.g. Renault, Molemaker, McWilliams, et al., 2016) is not considered in the ECMWF forecast model. Therefore, the ECMWF wind does not contain the imprint of the surface currents.

The SWOT WindWave dataset provides a product called *wind_speed_model* based on ECMWF analyses. In this study, we chose to use the forecast product instead because differences in wind speeds between the ECMWF forecast and SWOT provide information on how numerical models are able to simulate the atmospheric response to fine oceanic scales. In fact, differences will arise from both the spatial resolution of the atmospheric model or the spatial resolution of the ocean. The forecast used was run from 12:00 UTC on May 12 and we examine the output at 22:00 UTC. This ensures that the forecast had time to decorrelate from the analysis and from the observations (such as scatterometers) used to generate it. It will therefore reflect in a large part the response of the atmosphere to the ocean at the resolution of the coupled model.

In this study, we also use SST data from NOAA's Advanced Very High Resolution Radiometer (AVHRR L2p) with a spatial resolution of 1.1 km at nadir at 01:40 UTC on May 13 . We found that clouds were particularly absent at that time, allowing us to quantify the variability of the ocean on scales of a few kilometers. Finally, for visual comparison, we also examine chlorophyll concentration from the 4 km resolution L3 daily product Copernicus-GlobColor as well as the SSH anomaly provided by SWOT (L3 product, v.1.0.2, ssha_noiseless).

3 Results

3.1 Spatial structures

Figure 1 highlights the study area near Cape Hatteras, where the Gulf Stream separates from the coast. The Gulf Stream is a strong, deep, and persistent western boundary current that shapes our climate (Chassignet & Marshall, 2008; Minobe et al., 2008; Marshall & Coauthors, 2009; Renault, Molemaker, Gula, et al., 2016). As shown by both ECMWF and satellite observations (Fig. 1a and b, respectively), the Gulf Stream induces a pronounced SST gradient that separates advected warmer waters on its equatorial side from cooler waters on its poleward side. The region is also known to be characterized by strong mesoscale fronts, eddies, and submesoscale filaments and fronts (Gula et al., 2014; Callies et al., 2015). It is also prone to exceptionally strong air-sea interactions, with the largest heat transfer to the atmosphere over the global ocean (Josey et al., 1999; Czaja et al., 2019) and strong mesoscale coupling coefficients (Renault et al., 2019). Our analysis focuses on May, a month during which this region has previously been identified as a hotspot for pronounced MABL responses to oceanic conditions during the warm season (Sublette & Young, 1996).

Figure 1d shows the 10 m wind field from the ECMWF forecast at 22:00 UTC on May 12, *i.e.*, at about the same time as SWOT passes over the region (at 22:24 UTC). The surface winds blow northward with an anticyclonic curvature, with low winds (about 4 m s^{-1}) at latitudes around 34°N and higher winds (about 9 m s^{-1}) poleward. At this time, an elongated feature with winds lower than its surroundings can be observed, cen-

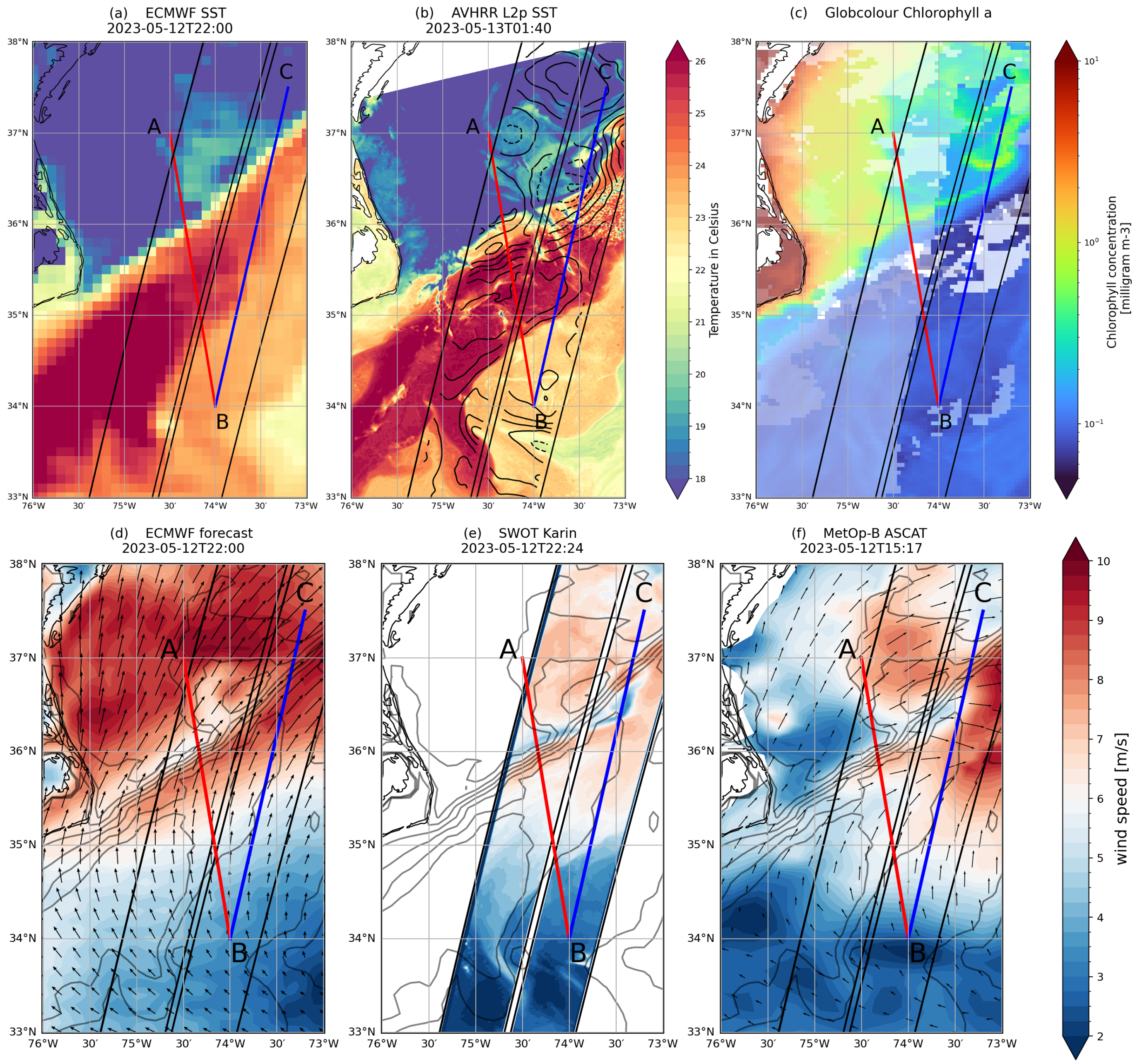

Figure 1. (a) Sea surface temperature from ECMWF forecast at 22:00 UTC on May 12 and (b) from AVHRR at 01:40 UTC on May 13. In (b) contours of SSH anomalies are overlaid (continuous contours for positive anomalies and dashed ones for negative ones); (c) Chlorophyll concentration from Copernicus-GlobColor, obtained by overlaying data from May 11, 12 and 13 were overlaid (see Fig. S3 of SI for the separate fields). (d) 10m wind speed of ECMWF forecast at 22:00 UTC, (e) SWOT wind speed at 22:24 UTC, (f) MetOp-B ASCAT wind speeds at 15:17 UTC, all on May 12. The correponding wind vectors have been added on panels (d) and (f). Note that SWOT does not provide wind directions. ECMWF SST is overlaid in black contours on panels (d-f).

tered around 36°N, 74.5°W, and oriented SW-NE. In the ECMWF product, its typical width is about 50km and it extends over 200km, with a wind anomaly of about 2 m s^{-1}. This situation is very close to that studied by Sublette and Young (1996), who described a case of strong imprint of the Gulf Stream on MABL in southwesterly conditions over the same spatial region. In particular, we note that the wind approximately blows along the SST front, which is known to favor a stronger response at both meso and submesoscale (Chelton et al., 2001; ONeill et al., 2012; Renault et al., 2019; Conejero et al., 2024).

As shown in Fig. 1e, the SWOT wind field is generally weaker than ECMWF forecast, which could be due to (ECMWF) model biases, but also to (SWOT) observational errors or calibration. However, despite these differences, the SWOT winds are in good agreement with ECMWF in terms of spatial structures. Thanks to its 2 km resolution, SWOT captures much finer details, revealing smaller-scale features that are not present in ECMWF. For example, the elongated low-wind structure observed in the ECMWF forecast is resolved with greater intricacy, showing a roll-up of the low-wind region with a minimum of about 4 m s^{-1} near 36.5°N, 73.5°W (see Fig. S1 of Supporting Information, SI, which is a close-up of this region). SWOT, in addition, identifies a unique feature not present in the ECMWF forecast near 34°N, 74.75°W - an elongated region with sharp wind speed gradients separating higher wind speeds (about 4.5 m s^{-1}) and weaker winds (about 2.5 m s^{-1}).

Finally, Figure 1f shows ASCAT winds at 15:17 UTC on May 12, with a comparison to winds at 02:35 UTC on May 13 in Fig. S2 of the SI. Across the region, the wind direction does not change much between these two dates while there is notable variations in the large-scale component of the wind speed. The low-wind elongated structure seen in both ECMWF and SWOT is captured by ASCAT, although the lower resolution of the scatterometer (∼25 km) cannot resolve the finer features observed by SWOT. The northeastward extension of the filament ends up around 36.5°N, 73.5°W, consistently with SWOT. The conspicuous elongated region near 34°N, 74.75°W can also be detected but with a lesser contrast in wind magnitude. This analysis highlights the ability of SWOT to capture finer wind features compared to coarser-resolution scatterometers and state-of-the-art forecast models.

For further investigation on the origin of these wind anomalies, the spatial distribution of SST in the same region is examined. Figure 1a shows the ECMWF SST field coinciding with the timing of the SWOT observations. A prominent SST front associated with the tongue of warm waters constituting the Gulf Stream is evident and extends from southwest to northeast, sharply delineating colder waters ($\sim$ 17°C) from warmer waters ($\sim$ 26°C). North of the front, a positive anomaly with uniform SST about $\sim$ 19.5°C and a diameter of about 100 km is identified at about 36.5°N, 74.25°W. This structure detaches from the front embedding a cold patch of a few tens of kilometers. However, the definition of the warm anomaly is limited by the coarse spatial resolution of the ECMWF model. South of the front, the Gulf Stream is characterized by a distinct tongue of warm waters and another front emerges that is predominantly southwest to northeast oriented, but shows a notable southward extrusion near 34°N, 74.75°W.

Figure 1b shows AVHRR SST obtained 3 hours after the SWOT measurements. We benefit from a cloud-free situation at this time, and the two data are relatively close in time to each other, so that AVHRR SST can be directly compared to the SWOT wind speed. In general, much more details can be seen with the AVHRR kilometer resolution compared to the ECMWF product. The SST anomaly centered at 36.5°N, 74.25°W with SST about 19.5°C, which had almost circular shape in the ECMWF product is still present, but with much finer details. Contrary to what could be inferred from ECMWF, the high-resolution SST (Fig. 1b) indicates that the 19.5°C SST feature is not attached on its southern side to the SST front of the Gulf Stream. In between, a cold filament 20 km wide extends over 100 km, with very high chlorophyll concentration (Fig. 1c). As the filament extends northeastward, it connects to a pouch of cold waters centered at about 36.5°N, 73.5°W. This feature, about 40 km wide and with a high chlorophyll concentration is trapped between regions of warmer waters.

The SSH provided by SWOT gives information on the ocean currents (see contours in Fig. 1b) The warm 19.5°C feature North of the Gulf Stream front is in fact associated with two cyclonic eddies (negative SST anomalies) centered at 37°N, 74.3°W, and 36.3°N, 73.5°W, This last one drives the advection of cold waters from the southwest, resulting in the formation of a narrow cold filament to its south and the pouch of cold water. It also facilitates the advection of warm water from the northeast. In addition, most of the SSH contours are closely aligned with the SST fronts, providing confidence that the AVHRR SST data at 01:40 UTC on May 13 are an accurate representation of the dynamics captured by SWOT at 22:24 UTC on May 12.

Focusing around the cold filament and the cold pouch to its NE, the correspondence between AVHRR SST (Fig. 1b) and SWOT wind speeds (Fig. 1e) is striking (see Fig. S1 in SI for a closer comparison). The elongated cold filament aligns with the minimum wind speed region, and the wrapping of small cold and warm anomalies to its northeast are similarly associated with regions of weaker and stronger winds, respectively. This highlights SWOT's ability to identify air-sea interactions with unprecedented resolution and to reveal that the atmosphere reacts to the ocean at scales of less than tens of kilometers. The discussion section will provide a possible interpretation of these results.

3.2 Transects

The tight visual correspondence between SST and wind speed anomalies is further analyzed using two transects. The first transect (B-A in Fig. 1a) crosses the cold filament observed in both the ECMWF and AVHRR SST datasets. The second transect (B-C) traverses the cold pouch at 36.5°N, 73.5°W, which spans less than 20 kilometers and is visible only in the AVHRR SST data. The comparison of these two transects allows to highlight the ability of a forecast model like IFS to capture the relationship between surface wind patterns and SST anomalies at fine scales.

Over the entire B-A transect, the ECMWF and AVHRR SST profiles are in agreement, with a relatively smoother profile for ECMWF due to its coarser spatial resolution (Fig. 2a). The transect crosses the Gulf Stream at about 36°N (see Fig. 1a), and both ECMWF and AVHRR SSTs drop from 26°C to 17°C. The finer resolution of AVHRR shows that the transect actually crosses two fronts, with a first SST drop of 3°C at about 35.65°N over 5 km, and then a second one of 6°C at about 36°N over 10 km. The minimum of SST near 36.25°N corresponds to the cold filament seen in Fig. 1b while the SST front at 34.75°N corresponds to the SW-NE extending tongue of warm water. In the ECMWF forecast, the wind generally increases over the transect from 4 m s^{-1} to 9 m s^{-1}, with a drop of about 2 m s^{-1} at 36°N, *i.e.*, at the same location as the SST front. The ASCAT winds at 15:17 UTC on May 12 and 02:35 UTC on May 13 both show a drop of about 2 m s^{-1} at 36°N, consistent with ECMWF forecast. Concerning SWOT, the wind speed measured by the instrument are in general agreement with the scatterometer winds north of 35°N. The differences occur close to the SST front, with a decrease in wind speed of about 2 m s^{-1} at 36°N occurring over 10 km for SWOT, whereas it occurs over 30 km for ASCAT. Also the region of wind speed minimum is thinner for SWOT (10 km). The

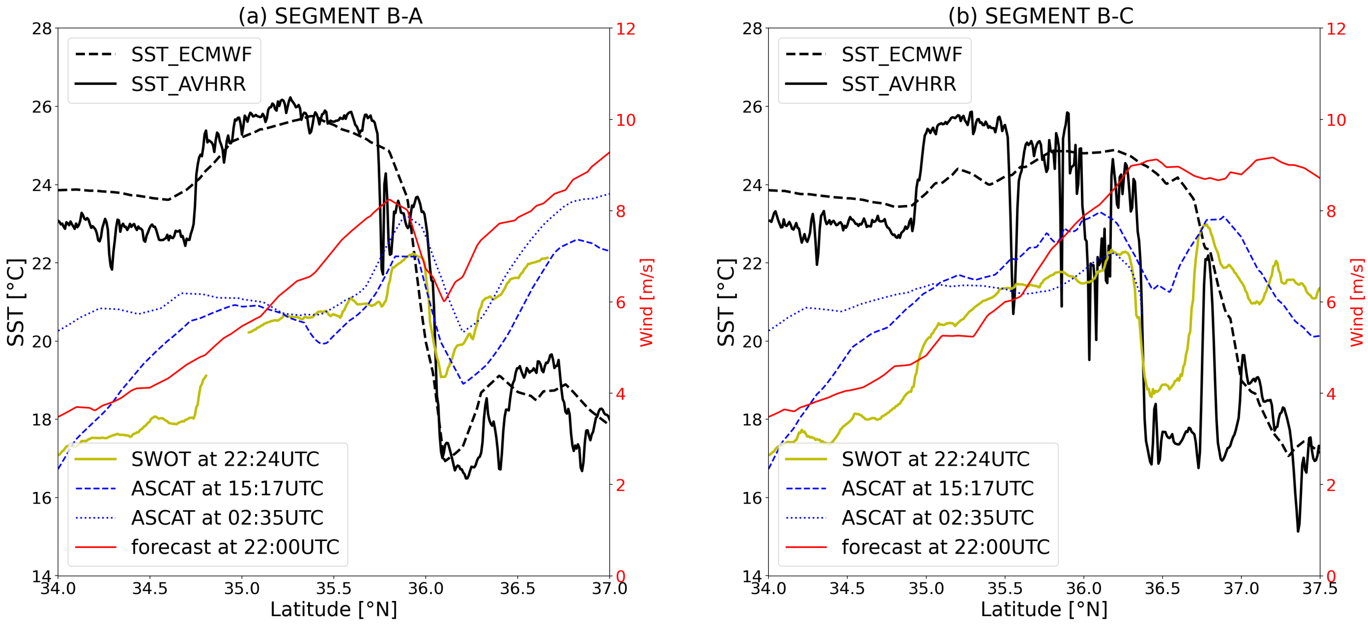

Figure 2. Transects B-A (panel a) and B-C (panel b) of wind speed and SST from various products. See Fig. 1b for definition of the transects. In panel (a), the curve corresponding to wind speed from SWOT is not continuous as the transect crosses the two swaths. In panel (b), there are no data for ASCAT north of 36.5°N at 2:35UTC (see swath on Fig. 1e).

relatively good agreement between ASCAT and SWOT at the lower range of mesoscales confirms the validity of the SWOT wind field product for understanding wind variations at such small scales. Finally, note that the southern SST front at 34.75°N associated with the warm water tongue is also concomitant with a wind increase at the same location. From these different results, we can evaluate the coupling coefficient between wind and SST by comparing the variation of wind speed to SST. For ECMWF we get a typical value of 0.25 m s^{-1}/C (drop of 2 m s^{-1} for 8°C). For SWOT and ASCAT, first the SST decreases by 3°C at 35.75°N with a wind speed increase of about 1 m s^{-1}, giving a typical value of 0.33 s^{-1} C^{-1}. Then the second drop of SST by 6°C occurs with a wind speed drop by 2 m s^{-1}, giving the same value. Such values for ASCAT and SWOT are in line with those found in the literature (e.g. ONeill et al., 2012; Gemmrich & Monahan, 2018).

We now examine the second transect, B-C (Fig. 2b), which intersects the submesoscale structures visible in the AVHRR SST image (Fig. 1b). There are clear differences between the SST profiles of the ECMWF and AVHRR products. The ECMWF SST profile shows a smooth, monotonic decrease between 36°N and 37.5°N. In contrast, the AVHRR data show a sharp SST drop of 7°C over 10 km at about 36.25°N (corresponding to the submesoscale pouch of cold waters), followed by an increase of 5°C over 5 km, and a further decrease further north. This corresponds to the cold filament that was observed on Fig. 1b. The ECMWF wind profile increases smoothly from south to north, with minimal variation on 50 km scales. On the contrary, ASCAT, measured at two different times, captures mesoscale variations, including a drop in wind speed of about 2 m s^{-1} near 36.4°N associated with the SST front. Compared to ASCAT and ECMWF, SWOT wind speed has sharper features with more important variations. For example, a 3 m s^{-1} drop over the SST front at 36.25°N can be seen in the SWOT data compared to the 2 m s^{-1} drop of ASCAT. There is a clear relation between SST small scale features and fronts and the SWOT wind speed variations. For instance, the SST front at 34.65°N is also evident with a wind speed front at the same location in the SWOT data. The submesoscale structure of 10 km width, associated with a warm SST anomaly at 36.75°N corresponds to a relative maximum in wind speed at the same location. Again, we can compute the coupling coefficient between wind speed and SST variations. The drop over the SST front corresponds to a coupling coefficient of about 0.28 m s^{-1} C^{-1} using ASCAT, while about 0.43 m s^{-1} C^{-1} using SWOT. Such large values using high-resolution data suggest that coupling coefficients may be underestimated when computed from standard scatterometer products or numerical models which resolve only variations at mesoscales.

4 Summary and discussion

Air-sea interactions have been documented through the analysis of the measurement of winds by scatterometers since a long time. The nominal spatial resolution of these satellite instruments is only 25 km, which does not allow to access to ocean submesoscale. Our study, based on different satellite observations in the Gulf Stream area, showed how surface winds, as measured the SWOT satellite, are correlated with SST anomalies down to a few kilometers. This opens new opportunities for the study of air-sea interactions at submesoscales.

One caveat of this study is related to the process of retrieving the wind field from the instrument backscatter. The Geophysical Model Function (GMF) used to compute surface winds does not include the SST effect (Stiles et al., 2024) and may distort our vision of a dynamical effect of SST on the MABL. Tran et al. (2023) studied the bias in wind speed as a function of SST using data from the AltiKa altimeter which is also a Ka-band instrument. From their Figure 1, we can estimate a bias of 0.05 m s^{-1}/C due to the dependence of the GMF to SST. This value is much smaller than the wind/SST coefficient about 0.3 m s^{-1}/C found in our study. This casts confidence that the observed correspondence between SST and wind speed anomalies at fine scales can be attributed to the effect of air-sea coupling. Note also that wind waves are not fully incorporated in the GMF as only ECMWF significant wave heights are used. We believe that taking the variability of waves would in fact accentuate the effect.

An additional source of uncertainty comes from the fact that, similar to scatterometers, the 10 m wind retrieved by SWOT represents the equivalent neutral wind relative to the oceanic currents (U_{ENWR}) rather than the actual wind (Plagge et al., 2012; Renault et al., 2019). Consequently, the fine spatial variation of the wind field observed by SWOT may also reflect the influence of surface currents. The absolute equivalent neutral wind, U_{ENW}, can be approximated as $U_{ENW} = U_{ENWR} + U_o$. The geostrophic surface currents, which can be inferred from the SWOT SSH data, reaches up to 1 m s^{-1} (Fig. S2). This could potentially modulate the wind response by up to 30%, either positively or negatively. However, this is an upper bound estimate, as the wind also responds to the surface current, and only a portion of the surface current should be considered in this context (see Renault et al., 2024).

A plausible candidate to explain the relation between SST and wind at the scales we consider is a sea-breeze circulation related to the differential heating of the ocean above the Gulf Stream (Hsu, 1984; Wai & Stage, 1989; Sublette & Young, 1996). Figure 3a presents the ECMWF surface heat fluxes at 22:00 UTC on May 12, which reveal to be positively correlated with SST at mesoscale. Strong gradients of heat fluxes are seen along the Gulf Stream front, separating the cold flank of the front, where the fluxes are only of the order of a few tens of W m^{-2}, from the warm flank, where fluxes are of the order of 200 W m^{-2}. These fluxes may allow a solenoidal circulation above the Gulf Stream front and other SST gradients, with vertical motions above large heating on the atmosphere. However surface divergence from the ECMWF model (Fig. 3b) shows instead ascent over the SST front of the Gulf Stream. These convergence motions just above SST gradients indicate that there is no solenoidal circulation which would instead lead to ascent and descent above each side of the front.

A second candidate would be related to the Pressure Adjustment Mechanism (PAM) (Lindzen & Nigam, 1987; Lambaerts et al., 2013) which is based on a thermal adjustment to the SST anomaly: a positive SST anomaly leads to a lower hydrostatic pressure, which causes the surface wind to converge. Again, one would expect ascent on the warm flank of the Gulf Stream and descent on the cold flank (Minobe et al., 2008)

The strong heating of the atmosphere by the ocean a differential stability of the MABL: more stable conditions over warm anomalies and unstable ones over cold anomalies. The vertical momentum mixing (VMM) (Hayes et al., 1989; Wallace et al., 1989) consists of an increase in turbulence in the boundary layer which causes winds to accelerate above positive SST anomalies. This is indeed seen for the different transects in Fig. 2. Another consequence of VMM is that strong convergence is to be found when winds blow in the opposite direction of the SST gradient (O'Neill et al., 2003; Chelton et al., 2004; Desbiolles et al., 2016). Indeed, along the Gulf Stream front, wind is partially blowing from the South, *i.e.*, from warm waters (see Fig. 1d). This is consistent with Fig. 3b, which shows that there is indeed a strong convergence of surface winds above the SST front. We therefore conclude that the VMM may explain a large part of the correlation between wind and SST anomalies, even at submesoscales for the particular situation we consider. An interesting point is that this correlation lasts for several hours as it can be spotted for the preceding and following passes of SWOT (10:00 UTC on May 12 and 10:00 UTC on May 13, see Fig. S4 in SI). Presumably, the strong difference in surface heat fluxes (in terms of tens of W/m^2) is responsible of the persistence of this phenomenon.

Finally, contrary to scatterometers, SWOT does not provide the wind direction. As shown by O'Neill et al. (2010), spatial variation of wind direction is also affected by mesoscale SST gradients. As a result, SWOT data alone cannot be used to compute wind divergence and wind curl and look at their correlation with down-wind and cross-wind SST gradients. New missions such as ODYSEA (Rodríguez et al., 2018; Torres et al., 2023; Larraaga et al., 2025) and analysis of the data of DopplerScat from the S-MODE campaign (Wineteer et al., 2024) could help to investigate these questions for submesoscales.

Open Research

The SWOT products used in this manuscript are freely distributed by mirror centers from NASA and CNES. The SWOT Level 2 KaRin Low Rate Wind Wave Data Prod-

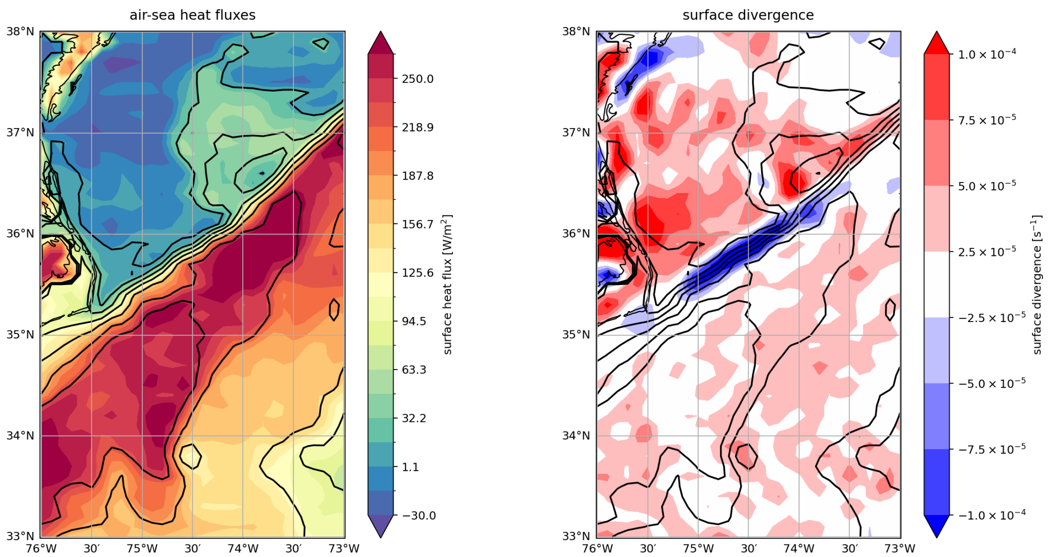

Figure 3. In color shadings, (a) ECMWF surface heat fluxes (sensible + latent) , (b) surface divergence at 22:00 UTC on May 12. In both panels, ECMWF SST is represented by black contours.

uct is available in SWOT Project (2023). The product quality is not final and will be affected by some evolutions as the SWOT project team makes progress on science data processing algorithms and instrument calibrations. The SWOT Level 3 KaRin Low Rate Sea Surface Height Data Unsmoothed Data Product is available in AVISO/DUACS (2024). It is made freely available by AVISO and DUACS teams as part of the DESMOS Science Team project.

MetOp-B ASCAT winds products are provided by EUMETSAT/OSI SAF (2018). The SST data is provided by Group for High Resolution Sea Surface Temperature (GHRSST) and the National Oceanic and Atmospheric Administration (NOAA/STAR, 2023). The Copernicus-GlobColour product was obtained from the Copernicus Marine Service repository (2024).

Acknowledgments

This work is a contribution to the joint projects I-CASCADE and POSEIDON funded by the French CNES TOSCA program. M. K. is supported by a PhD grant funded by CNES and Sorbonne Université. We acknowledge CNES for awarding access to its HPC resources.

Author contributions: M.K.: Formal Analysis, Investigation, Methodology, Software, Visualization, Writing, Original Draft Preparation, Review & Editing. G. L.: Conceptualization, Formal Analysis, Investigation, Methodology, Writing, Original Draft, Review & Editing, Funding Acquisition. L. R.: Investigation, Writing - Review & Editing, Funding Acquisition. X.P.: Data curation and Resources. C.D.: Formal Analysis.

References

AVISO/DUACS. (2024). *Level-3 KaRIn Low Rate SSH Unsmoothed (v1.0.1)* [Dataset]. doi: 10.24400/527896/A01-2024.003

Bai, Y., Thompson, A. F., Villas-Bas, A. B., Klein, P., Torres, H. S., & Menemenlis, D. (2023). Sub-mesoscale wind-front interactions: The combined impact of thermal and current feedback. *Geophys. Res. Lett.*, *50*, e2023GL104807.

Callies, J., Ferrari, R., Klymak, J. M., & Gula, J. (2015). Seasonality in submesoscale turbulence. *Nature Comm.*, *6*, 6862.

Capet, X., Mcwilliams, J. C., Molemaker, M. J., & Shchepetkin, A. F. (2008). Mesoscale to submesoscale transition in the California Current System. Part III: Energy balance and flux. *J. Phys. Oceanog.*, *38*, 2256–2269.

Chassignet, E. P., & Marshall, D. P. (2008). Gulf Stream separation in numerical ocean models. In *Ocean modeling in an eddying regime* (p. 39-61). American Geophysical Union (AGU).

Chelton, D. B., Esbensen, S. K., Schlax, M. G., Thum, N., Freilich, M. H., Wentz, F. J., ... Schopf, P. S. (2001). Observations of coupling between surface wind stress and sea surface temperature in the eastern tropical Pacific. *J. Climate*, *14*, 1479–1498.

Chelton, D. B., Schlax, M. G., Freilich, M. H., & Millif, R. F. (2004). Satellite measurements reveal persistent small-scale structures in ocean winds. *Science*, *303*, 978.

Conejero, C., Renault, L., Desbiolles, F., McWilliams, J. C., & Giordani, H. (2024). Near-surface atmospheric response to meso- and submesoscale current and thermal feedbacks. *J. Phys. Oceanogr.*, *54*, 823–848.

Copernicus Marine Service repository. (2024). *Copernicus-GlobColour* [[Dataset] CMEMS]. doi: 10.48670/moi-0028

Czaja, A., Frankignoul, C., Minobe, S., & Vannière, B. (2019). Simulating the midlatitude atmospheric circulation: What might we gain from high-resolution modeling of air-sea interactions? *Current Climate Change reports*, *5*, 390–406.

Desbiolles, F., Blanke, B., Bentamy, A., & Roy, C. (2016). Response of the Southern Benguela upwelling system to fine-scale modifications of the coastal. w.ind. *J. Marine Sys.*, *156*, 46–55.

EUMETSAT/OSI SAF. (2018). *MetOp-B ASCAT Level 2 Ocean Surface Wind Vectors Optimized for Coastal Ocean. Version Operational/Near-Real-Time* [Dataset]. doi: 10.15770/EUM_SAF_OSI_NRT_2018

Fu, L.-L., Pavelsky, T., Cretaux, J.-F., Morrow, R., Farrar, J. T., Vaze, P., ... Dibarboure, G. (2024). The Surface Water and Ocean Topography Mission: A breakthrough in radar remote sensing of the ocean and land surface water. *Geophys. Res. Lett.*, *51*, e2023GL107652.

Gaube, P., Chickadel, C. C., Branch, R., & Jessup, A. (2019). Satellite observations of SST-induced wind speed perturbation at the oceanic submesoscale. *Geophys. Res. Lett.*, *46*, 2690–2695.

Gemmrich, J., & Monahan, A. (2018). Covariability of near-surface wind speed statistics and mesoscale sea surface temperature fluctuations. *J. Phys. Oceanogr.*, *48*, 465–478.

Gula, J., Molemaker, M. J., & McWilliams, J. C. (2014). Submesoscale cold filaments in the Gulf Stream. *J. Phys. Oceanog.*, *44*, 2617–2643.

Hayes, S. P., McPhaden, M. J., & Wallace, J. M. (1989). The influence of sea surface temperature on surface wind in the eastern equatorial Pacific: weekly to monthly variability. *J. Climate*, *2*, 1500-1506.

Hsu, S. A. (1984). Sea-breeze-like winds accross the north wall of the Gulf Stream: an analytical model. *J. Geophys. Res.*, *89*, 2025–2028.

Josey, S. A., Kent, E. C., & Taylor, P. K. (1999). New insights into the ocean heat budget closure problem from analysis of the SOC air–sea flux climatology. *J. Climate*, *12*, 2856–2880.

Klein, P., Hua, B. L., Lapeyre, G., Capet, X., Gentil, S. L., & Sasaki, H. (2008). Upper ocean turbulence from high 3-D resolution simulations. *J. Phys. Oceanogr.*, *38*, 1748–1763.

Klein, P., & Lapeyre, G. (2009). The oceanic vertical pump induced by mesoscale and submesoscale turbulence. *Ann. Rev. Marine Sci.*, *1*, 351–375.

Klein, P., Lapeyre, G., Siegelman, L., Qiu, B., Fu, L.-L., Torres, H., ... Gentil, S. L. (2019). Ocean scale interactions from space. *Earth. Space. Sci.*, *6*, 795–817.

Lambaerts, J., Lapeyre, G., Plougonven, R., & Klein, P. (2013). Atmospheric response to sea surface temperature mesoscale structures. *J. Geophys. Res.*, *118*, 9611–9621.

Larraaga, M., Renault, L., Wineteer, A., Contreras, M., Arbic, B. K., Bourassa, M. A., & Rodriguez, E. (2025). Assessing the future ODYSEA satellite mission for the estimation of ocean surface currents, wind stress, energy fluxes, and the mechanical coupling between the ocean and the atmosphere. *Remote Sens.*, *17*, 302.

Lévy, M., Franks, P. J. S., & Smith, K. S. (2018). The role of submesoscale currents in structuring marine ecosystems. *Nature Comm.*, *9*, 4758.

Lindzen, R. S., & Nigam, S. (1987). On the role of sea surface temperature gradients in forcing low level winds and convergence in the tropics. *J. Atmos. Sci.*, *44*, 2418–2436.

Marshall, T. C. G. J., & Coauthors. (2009). The climode field campaign: Observing the cycle of convection and restratification over the gulf stream. *Bull. Amer. Meteor. Soc.*, *90*, 1337-1350.

McWilliams, J. C. (2016). Submesoscale currents in the ocean. *Proc. Roy. Soc. London Ser. A*, *472*, 20160117.

Minobe, S., Kuwano-Yoshida, A., Komori, N., Xie, S.-P., & Small, R. J. (2008). Influence of the Gulf Stream on the troposphere. *Nature*, *452*, 206–209.

Morrow, R., Fu, L.-L., Ardhuin, F., Benkiran, M., Chapron, B., Cosme, E., ... Zaron, E. D. (2019). Global observations of fine-scale ocean surface topography with the Surface Water and Ocean Topography (SWOT) mission. *Front. Mar. Sci.*, *6*, 232.

NOAA/STAR. (2023). *GHRSST L2P Metop-C AVHRR FRAC ACSPO v2.80 1km Dataset. Ver. 2.80. PO.DAAC, CA, USA* [Dataset]. doi: 10.5067/GHMTC-2PS28

O'Neill, L. W., Chelton, B., & Esbensen, S. K. (2010). The effects of sst-induced surface wind speed and direction gradients on midlatitude surface vorticity and divergence. *J. Climate*, *23*, 255–281.

O'Neill, L. W., Chelton, D. B., & Esbensen, S. K. (2003). Observations of SST-induced perturbations of the wind stress field over the southern ocean on seasonal timescales. *J. Climate*, *16*, 2340–2354.

ONeill, L. W., Chelton, D. B., & Esbensen, S. K. (2012). Covariability of surface wind and stress responses to sea surface temperature fronts. *J. Climate*, *25*, 5916–5942.

Plagge, A. M., Vandemark, D., & Chapron, B. (2012). Examining the impact of surface currents on satellite scatterometer and altimeter ocean winds. *J. Atmos. Ocean. Technol.*, *29*, 1776–1793.

Renault, L., Contreras, M., Marchesiello, P., Conejero, C., Uchoa, I., & Wenegrat, J. (2024). Unraveling the impacts of submesoscale thermal and current feedbacks on the low-level. w.inds and oceanic submesoscale currents. *J. Phys. Oceanog.*, *54*, 2463–2486.

Renault, L., Masson, S., Oerder, V., Jullien, S., & Colas, F. (2019). Disentangling the mesoscale ocean-atmosphere interactions. *J. Geophys. Res. Oceans*, *124*, 2164–2178.

Renault, L., Molemaker, M. J., Gula, J., Masson, S., & McWilliams, J. C. (2016). Control and stabilization of the Gulf Stream by oceanic current interaction with the atmosphere. *J. Phys. Oceanogr.*, *46*, 3439–3453.

Renault, L., Molemaker, M. J., McWilliams, J. C., Shchepetkin, A. F., Lemarié, F., Chelton, D., … Hall, A. (2016). Modulation of wind work by oceanic current interaction with the atmosphere. *J. Phys. Oceanogr.*, *46*, 1685–1704.

Rodríguez, E., Wineteer, A., Perkovic-Martin, D., Gál, T., Stiles, B. W., Niamsuwan, N., & Rodriguez Monje, R. (2018). Estimating ocean vector winds and currents using a ka-band pencil-beam doppler scatterometer. *Remote Sens.*, *10*, 576.

Shao, M., Ortiz-Suslow, D. G., Haus, B. K., Lund, B., Williams, J. N., zgkmen, T. M., … Klymak, J. M. (2019). The variability of winds and fluxes observed near submesoscale fronts. *J. Geophys. Res.*, *124*, 7756-7780.

Song, X., Xie, X., Qiu, B., Cao, H., Xie, S.-P., Chen, Z., & Yu, W. (2022). Air-sea latent heat flux anomalies induced by oceanic submesoscale processes: An observational case study. *Front. Mar. Sci.*, *9*, 850207.

Stiles, B. W., Fore, A. G., Bohe, A., Chen, A. C., Chen, C. W., Molero, B., & Dubois, P. (2024). Ocean surface wind speed retrieval for SWOT Ka-band radar interferometer. In *IGARSS 2024 - 2024 IEEE International Geoscience and Remote Sensing Symposium* (p. 1422-1425).

Strobach, E., Klein, P., Molod, A., Fahad, A. A., Trayanov, A., Menemenlis, D., & Torres, H. (2022). Local air-sea interactions at ocean mesoscale in western boundary currents. *Geophys. Res. Lett.*, *49*, e2021GL097003.

Su, Z., Wang, J., Klein, P., Thompson, A. F., & Menemenlis, D. (2018). Ocean submesoscales as a key component of the global heat budget. *Nature Comm.*, *9*, 775.

Sublette, M. S., & Young, G. S. (1996). Warm-season effects of the Gulf Stream on mesoscale characteristics of the atmospheric boundary layer. *Mon. Weather Rev.*, *124*, 653–667.

SWOT Project. (2023). *Level-2 KaRIn Low Rate WindWave (v2.0)* [Dataset]. doi: 10.24400/527896/A01-2023.014

Taylor, J. R., & Thompson, A. F. (2023). Submesoscale dynamics in the upper ocean. *Annu. Rev. Fluid Mech.*, *55*, 103–127.

Torres, H., Wineteer, A., Klein, P., Lee, T., Wang, J., Rodriguez, E., ... Zhang, H. (2023). Anticipated capabilities of the ODYSEA wind and current mission concept to estimate wind work at the airsea interface. *Remote Sens*, *15*, 3337.

Tran, N., Vandemark, D., Bignalet-Cazalet, F., & Dibarboure, G. (2023). Quantifying multifrequency ocean altimeter wind speed errors due to sea surface temperature and resulting impacts on satellite sea level measurements. *Remote Sens.*, *15*, 3235.

Verhoef, A., Portabella, M., & Stoffelen, A. (2012). High-resolution ascat scatterometer winds near the coast. *IEEE Trans. on Geoscience and Remote Sensing*, *50*, 2481-2487.

Vivant, F., Siegelman, L., Klein, P., Torres, H. S., Menemenlis, D., & Molod, A. M. (2025). Ocean submesoscale fronts induce diabatic heating and convective precipitation within storms. *Commun. Earth Environ.*, *6*, 69.

Wai, M. M.-K., & Stage, S. A. (1989). Dynamical analysis of marine atmospheric boundary layer structure near the Gulf Stream oceanic front. *Q. J. R. Meteorol. Soc.*, *115*, 29-44.

Wallace, J. M., Mitchell, T. P., & Deser, C. (1989). The influence of sea surface temperature on surface wind in the eastern equatorial Pacific: seasonal and interannual variability. *J. Climate*, *2*, 1492–1499.

Wenegrat, J. O., & Arthur, R. S. (2018). Response of the atmospheric boundary layer to submesoscale sea-surface temperature fronts. *Geophys. Res. Lett.*, *45*, 13505–13512.

Wineteer, A., Rodriguez, E., Martin, D. P., Torres, H., Polverari, F., Akbar, R., & Rocha, C. (2024). Exploring the characteristics of ocean surface winds at high resolution with doppler scatterometry. *Geophys. Res. Lett.*, *51*, e2024GL113455.

Zhang, Z., Miao, M., Qiu, B., Tian, J., Jing, Z., Chen, G., ... Zhao, W. (2024). Submesoscale eddies detected by SWOT and moored observations in the Northwestern Pacific. *Geophys. Res. Lett.*, *51*, e2024GL110000.

Supporting Information for "Submesoscale air-sea interactions as revealed by SWOT"

M. Kaouah[1,2], G. Lapeyre[1], L. Renault[2], X. Perrot[1] and C. Dablemont[3]

[1]LMD-IPSL, ENS, PSL Université, CNRS, Paris, France

[2]Université de Toulouse, LEGOS (CNES/CNRS/IRD/UPS), Toulouse, France

[3]Institut des Sciences Moléculaires d'Orsay (ISMO), CNRS, Université Paris-Saclay, France

Contents of this file

Corresponding author: G. Lapeyre, LMD-IPSL, Ecole Normale Supérieure, 75005 Paris, France. (guillaume.lapeyre@sorbonne-universite.fr)

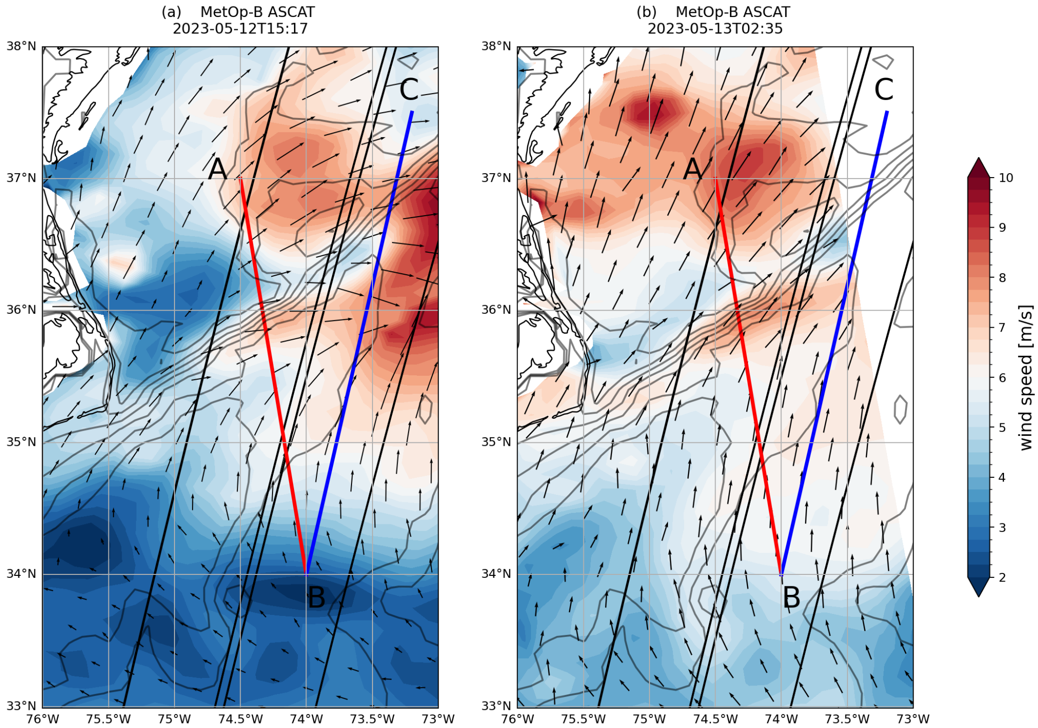

Figure S1. MetOp-B ASCAT wind speeds at (a) 15:17 on May 12 and (b) 02:35 on May 13. The corresponding wind vectors have been added on each panel. ECMWF SST is overlaid in black contours.

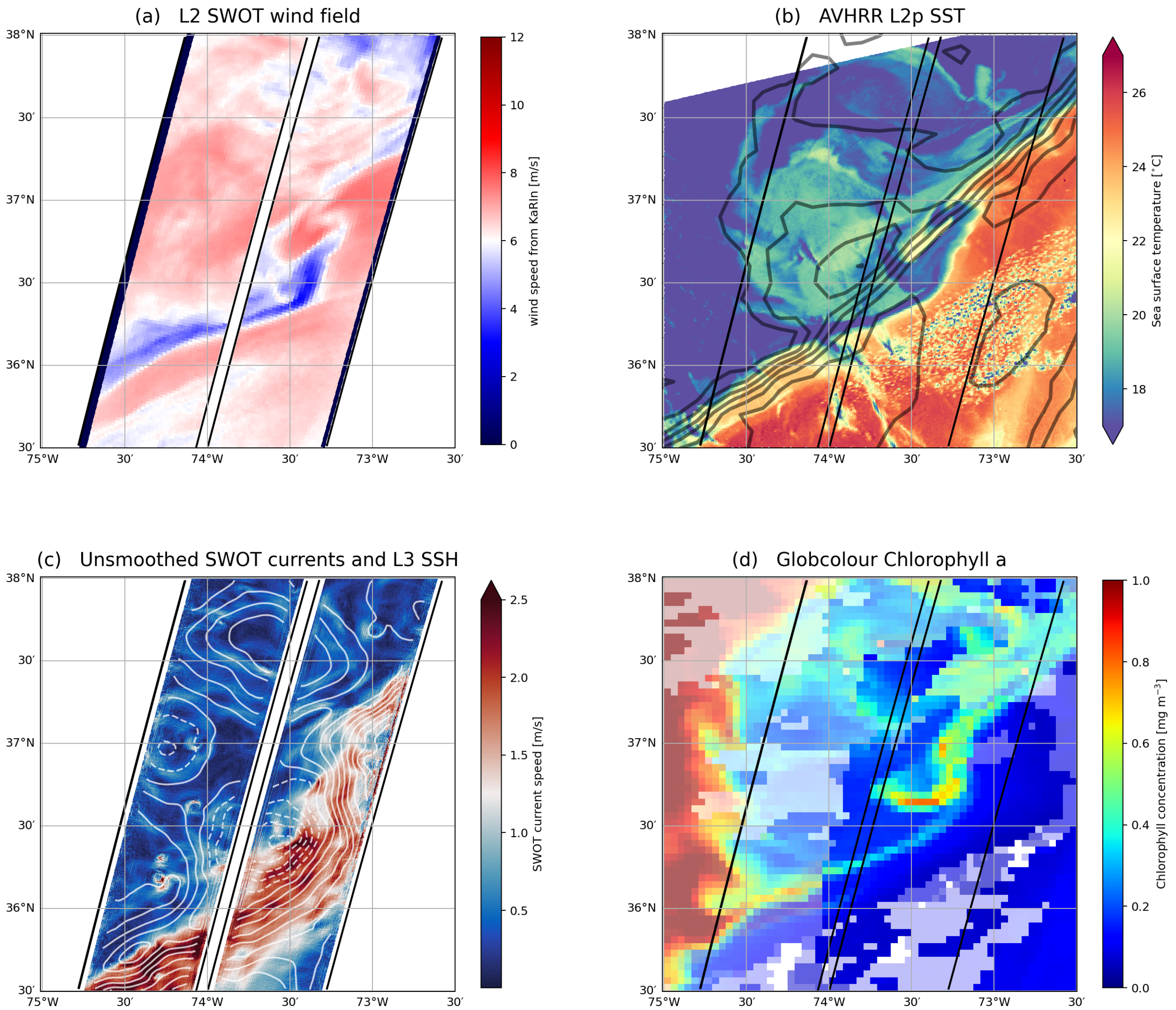

Figure S2. A close-up of different quantities near the cold pouch at 36.5°N, 73.5°W. (a) SWOT wind speed; (b) in color shadings, AVHRR SST and in black contours ECMWF SST. (c) 2 km L3 SSH and "Unsmoothed" L3 (250 m) ocean currents from SWOT. (d) Chlorophyll concentration using different snapshots (see Fig. S3). The "Unsmoothed" SSH is very similar to the 2km product, but the ocean currents come from the Unsmoothed L3 product as more submesoscale structures can be seen. The black lines allow to see the swaths of the satellite.

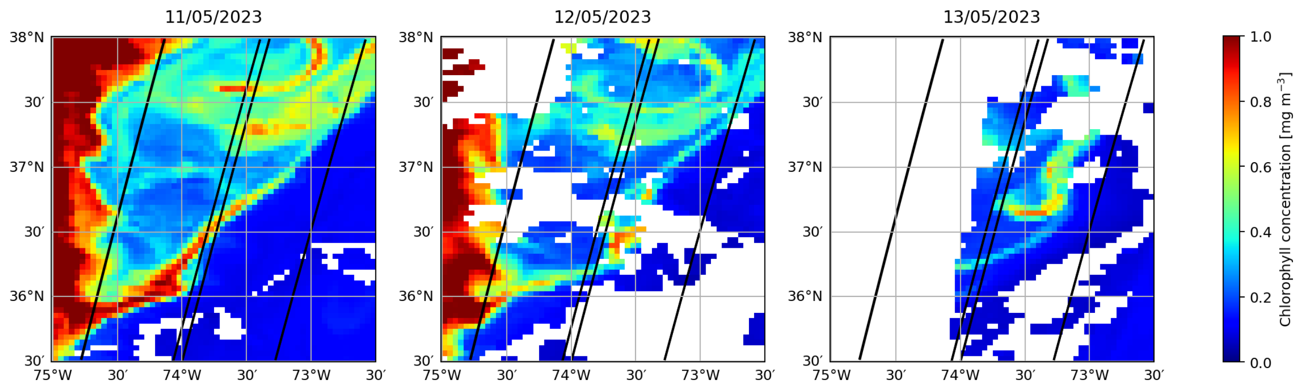

Figure S3. Chlorophyll concentration at different times, used to produce Fig. 1c of the paper and Fig. S1b.

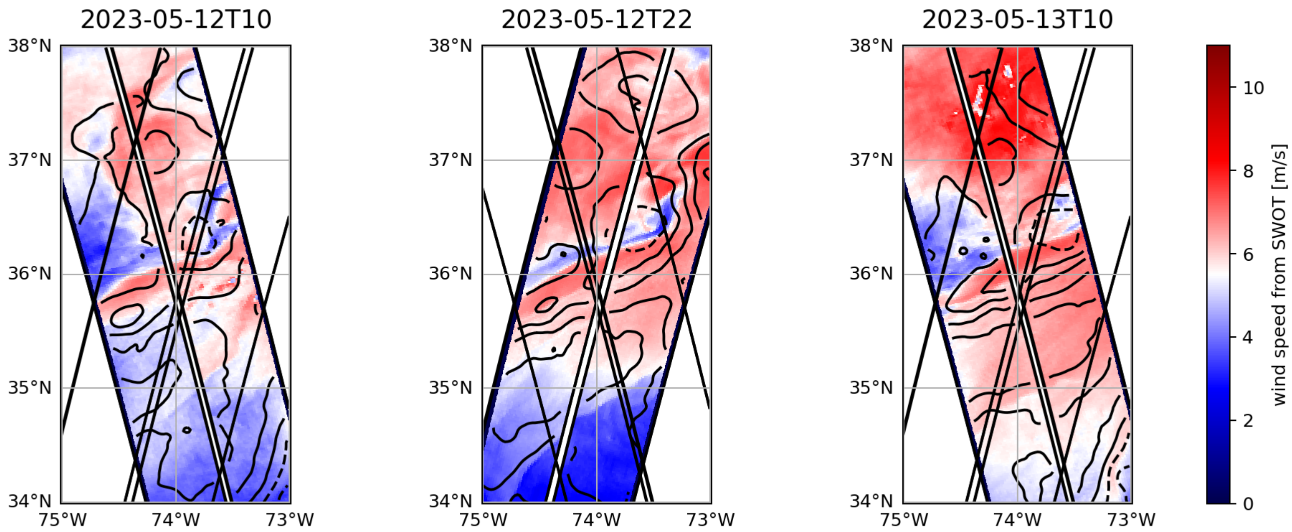

Figure S4. Evolution of wind speed as seen by SWOT. SSH anomalies are overlaid. The weaker wind speed associated to the cold filament persists over 1 day.